Research in Astronomy and Astrophysics, 24:095009 (13pp), 2024 September https://doi.org/10.1088/1674-4527/ad6bd5

The Energy Sources and the Explosion Mechanism of Ca-rich Supernova PTF 10iuv

Qiu-Ping Huang (黄秋萍)[1], Shan-Qin Wang (王善钦)[1], Tao Wang (王涛)[2], Wen-Pei Gan (甘文沛)[3], Deng-Wang Shi (石登旺)[1], Liu-Yi Wang (王浏毅)[1], and En-Wei Liang (梁恩维)[1]
[1] Guangxi Key Laboratory for Relativistic Astrophysics, School of Physical Science and Technology, Guangxi University, Nanning 530004, China; shanqinwang@gxu.edu.cn
[2] Department of Astronomy, Beijing Normal University, Beijing 100875, China
[3] Nanjing Hopes Technology Co., Ltd., Nanjing 210000, China
Received 2024 May 9; revised 2024 July 22; accepted 2024 July 24; published 2024 September 16

Abstract

In this paper, we perform the detailed modeling for the light curves (LCs) of PTF 10iuv which is a calcium-rich (Ca-rich) supernova (SN) to constrain the physical properties of its ejecta and the energy sources, as well as the explosion mechanism. We find that the ^{56}Ni model and the ^{56}Ni plus circumstellar interaction model fail to explain the LCs, while the four-element (^{56}Ni, ^{48}Cr, ^{52}Fe, and ^{44}Ti) model can account for the LCs. The ejecta mass of PTF 10iuv derived by the model ($1.52^{+0.34}_{-0.25}\ M_{\odot}$) is consistent with that of the merger of a sub-Chandrasekhar mass white dwarf. The early-time LCs were mainly powered by ^{56}Ni whose mass is $\sim$0.03 $M_{\odot}$, while the contributions of ^{48}Cr and ^{52}Fe can be neglected. The derived ^{44}Ti mass ($\sim$0.25 $M_{\odot}$) is $\sim$1.8 times the upper limit of the derived ^{44}Ti mass of Ca-rich SN 2005E. We suggest that subtracting the contributions of the host-galaxy, which are unknown, and including the flux from other long-lived elements (e.g., ^{57}Co, ^{55}Fe, ^{60}Co) can reduce the amount of ^{44}Ti, and that this value can be regarded as an upper limit.

Key words: (stars:) supernovae: general – (stars:) supernovae: individual (PTF 10iuv) – (stars:) novae – cataclysmic variables

1. Introduction

Supernovae (SNe) are the explosions of white dwarfs (WDs) in binary systems or aged massive stars. According to their spectra at photospheric phases, most SNe can be divided into types: Ia, Ib, Ic, IIb, and II (Filippenko 1997, a more detailed classification scheme can be found in Gal-Yam 2017). It is widely believed that type Ia SNe are from the explosions of WDs, while most of the other sub-types are from the explosions of massive stars.

Over the past two decades, a few dozen new optical transients, which were classified as calcium-rich (Ca-rich) SNe or transients, have been confirmed (e.g., Filippenko et al. 2003; Kawabata et al. 2010; Perets et al. 2010; Sullivan et al. 2011; Kasliwal et al. 2012; Valenti et al. 2014; Lunnan et al. 2017; De et al. 2018, 2020; Lee et al. 2019; Jacobson-Galán et al. 2020b). Although the spectra of most confirmed Ca-rich SNe at the photospheric phases can also be divided into types Ia (SN 2016hnk, SN 2019ofm, Jacobson-Galán et al. 2020a; De et al. 2020), Ib (e.g., SN 2005E, SN 2005cz, SN 2007ke, PTF 10iuv, PTF 11kmb, Puckett & Dowdle 2000; Aazami & Li 2001; Filippenko et al. 2003; Puckett et al. 2003; Pugh & Li 2003; Dimai et al. 2005; Graham et al. 2005; Chu et al. 2007; Perets et al. 2010; Kasliwal et al. 2012; Foley 2015; Lunnan et al. 2017; De et al. 2018, 2020; Jacobson-Galán et al. 2020a, 2020b; Ertini et al. 2023), Ic (SN 2012hn, SN 2018gwo, SN 2022oqm, Valenti et al. 2014; De et al. 2020; Irani et al. 2024), and IIb (iPTF15eqv, SN 2018jak, SN 2019ehk, SN 2020sbw, SN 2021M, SN 2021pb, SN 2021sjt, Cao et al. 2015; De et al. 2021; Das et al. 2023),[4] their late-phase nebular spectra show prominent calcium (Ca) and weak oxygen (O) lines, which are distinct from those of normal SNe Ia, Ib, Ic, and IIb (see Taubenberger 2017).

The explosion sites of Ca-rich SNe are also different from those of normal SNe Ib and Ic. In contrast to SNe Ib and Ic which were found in star-forming regions, almost all Ca-rich SNe are in old environments which are far from the center of their (potential) host galaxies (see Taubenberger (2017) and references therein).

Additionally, most Ca-rich SNe have fast-evolving light curves (LCs), indicating that their ejecta masses ($M_{\rm ej}$) are rather small, comparable to those of some ultra-stripped-envelope SNe Ic (e.g., SN 2005ek, Drout et al. 2013). Perets et al. (2010) find that the ejecta mass of SN 2005E is $\approx 0.3 \pm 0.1\ M_{\odot}$, and suggest that the ejecta was from the ejected helium shell surrounding a WD. To our knowledge, all confirmed Ca-rich SNe are low-luminosity cases with peak absolute magnitudes

[4] Additionally, there are several Ca-rich SNe whose spectral types are unknown (PTF 09dav, PTF 11bij, PTF 12bho, SN 2019bkc, SN 2019pof, Sullivan et al. 2011; Chen et al. 2020; Prentice et al. 2020).

between −14 and −17.5 mag. Assuming that the LCs of Ca-rich SNe are powered by the cascade decay of radioactive elements, the low peak-luminosities mean that the total masses of the radioactive elements synthesized are significantly lower than those produced by normal SNe Ib and Ic.

The features of Ca-rich SNe challenge the standard scenarios of SN explosions. For instance, the progenitors of normal SNe Ib and Ic are believed to be massive stars, but the progenitors of Ca-rich SNe Ib are suggested to be WDs in binary systems (Perets et al. 2010; Lyman et al. 2014; Foley 2015; Lunnan et al. 2017; Zenati et al. 2023). Furthermore, the numerical simulations (Bildsten et al. 2007; Shen & Bildsten 2009; Shen et al. 2010; Waldman et al. 2011; Woosley & Kasen 2011) suggest that explosions of sub-Chandrasekhar mass WDs can reproduce some features (low peak luminosities, low ejecta masses, high abundance of Ca, and so on) of Ca-rich SNe Ib.

Though the explosion mechanisms and progenitor systems of Ca-rich SNe are still elusive, it is possible to constrain the physical parameters of Ca-rich SNe and infer their energy sources. Some groups (e.g., Kasliwal et al. 2012; De et al. 2018, 2020) use the ^{56}Ni cascade decay (^{56}Ni → ^{56}Co → ^{56}Fe) model to estimate $M_{\rm ej}$, ^{56}Ni masses ($M_{\rm Ni}$), and other explosion parameters.

However, the assumption that the LCs of Ca-rich SNe were solely powered by ^{56}Ni cascade decay is not always valid for Ca-rich SNe. The studies for the nucleosynthesis of SN 2005E (Perets et al. 2010) and the explosions of sub-Chandrasekhar mass WDs (Bildsten et al. 2007; Shen & Bildsten 2009; Shen et al. 2010; Waldman et al. 2011; Woosley & Kasen 2011) show that some other short-lived radioactive elements (e.g., ^{52}Fe, ^{48}Cr) and long-lived radioactive elements (e.g., ^{44}Ti) should also be produced by Ca-rich SNe. Jacobson-Galán et al. (2021) use a radioactive model including the contributions of ^{56}Co and ^{57}Co which are from the decay of ^{56}Ni and ^{57}Ni to fit the late-time bolometric LC of Ca-rich SN 2019ehk, obtaining the ^{56}Co mass and constraining the upper limit of ^{57}Co mass. In several numerical models, the ^{56}Ni masses can be as low as 10^{-7}–10^{-4} $M_\odot$, which are significantly lower than ^{48}Cr masses in the same models (Waldman et al. 2011). In these models, the contribution of cascade decay of ^{48}Cr (^{48}Cr → ^{48}V → ^{48}Ti) is significantly larger than that of ^{56}Ni at the early epochs (see, e.g., Figure 4 of Waldman et al. 2011). Besides, the amount of ^{44}Ti synthesized in the explosions of sub-Chandrasekhar mass WDs can be up to $\sim 10^{-1}$ $M_\odot$ (Perets et al. 2010; Waldman et al. 2011; Zenati et al. 2023), 3−4 order of magnitude larger than the mass of ^{44}Ti ($M_{\rm Ti}$) from core-collapse SNe (CCSNe, $1-15\times 10^{-5}$ $M_\odot$, Timmes et al. 1996) and SNe Ia ($0.87–2.7\times 10^{-5}$ $M_\odot$, The et al 2006). Although the contribution of the cascade decay of ^{44}Ti (^{44}Ti → ^{44}Sc → ^{44}Ca) can be neglected in early-time LCs of SNe, it can change the shapes of the LCs of some Ca-rich SNe as early as ∼100 days and dominate the late-time LCs (see, e.g., Figure 4 of Waldman et al. 2011).

In this paper, we perform a theoretical study for PTF 10iuv (=SN 2010et) (Kasliwal et al. 2012) which is one of Ca-rich SNe that was observed over 200−300 days. PTF 10iuv was detected by the Palomar Transient Factory (PTF) at a redshift (z) of 0.023 on 2010 May 31, when its r–band magnitude was 21.2 (see Kasliwal et al. 2012; Dessart & Hillier 2015; Moriya et al. 2017 and references therein). Follow up photometric observations for PTF 10iuv were performed by using *Bgriz* filters of the Palomar 60 inch telescope (P60), the Large Format Camera (LFC) on the Palomar 200 inch telescope (P200), and the Low Resolution Imaging Spectrometer (LRIS) on the Keck I telescope. The r–band LC peaked to 19.0 mag in 10 days, and declined rapidly (1 magnitude within 12 days) (Kasliwal et al. 2012). One month later, PTF 10iuv evolved slowly at the rate of 0.02 mag day^{-1} for three months followed by a declined rate of 0.005 mag day^{-1}. The spectra of PTF 10iuv signify that it is a Ca-rich SNe Ib. The distance of PTF 10iuv from the nearest galaxy which might be its host galaxy is 37 kpc (Kasliwal et al. 2012).

Kasliwal et al. (2012) use the input power function of the ^{56}Ni cascaded decay to fit the r–band LC of PTF 10iuv, finding that the flux of late-time data is brighter than that reproduced by ^{56}Ni cascaded decay. Kasliwal et al. (2012) suggest that the late-time excesses relative to the ^{56}Ni input luminosity might be due to host-galaxy contamination or the contributions from other radioactive elements, e.g., ^{44}Ti. As pointed out by Kasliwal et al. (2012), however, the ^{44}Ti mass required is ~ 2 $M_\odot$, if the late-time flux was powered solely by ^{44}Ti decay. Kasliwal et al. (2012) suggest that the modeling of the LCs of PTF 10iuv can better constrain the models including the contributions from ^{48}Cr, ^{44}Ti, and ^{52}Fe, since the photometry in the rising and late phases is available. However, the detailed modeling has not been performed. This is the aim of our study.

In Section 2, we use the ^{56}Ni model and other models which are more complicated than the ^{56}Ni model to fit the multi-band LCs of PTF 10iuv. In Section 3, we discuss the physical parameters and the possible implications. In Section 4, we draw some conclusions. Throughout this paper, we assume $\Omega_{\rm m}=0.315$, $\Omega_\Lambda=0.685$, $H_0=67.3$ km s^{-1} Mpc^{-1} (Planck Collaboration et al. 2014). The values of foreground Galactic reddening are from Schlafly & Finkbeiner (2011).

2. Modeling the Multi-band LCs of PTF 10iuv

In this section, we model the multi-band LCs of PTF 10iuv. In the photospheric phase, the bolometric luminosity of SNe is (see e.g., Arnett 1982; Chatzopoulos et al. 2012)

$$L_{\rm SN}(t)=\frac{2}{\tau_m}e^{-\frac{t^2}{\tau_m^2}}\int_0^t e^{\frac{t'^2}{\tau_m^2}}\frac{t'}{\tau_m}L_{\rm input}(t')dt', \quad (1)$$

where $L_{\rm input}(t)$ is the instantaneous power input, $\tau_m=(2\kappa M_{\rm ej}/\beta_{\rm SN}v_{\rm ph}c)^{1/2}$ is the diffusion timescale (Arnett 1982), κ is optical opacity of the ejecta whose value is in the range of 0.025–0.25 cm^2 g^{-1} (see, e.g., Mazzali et al. 2001), $v_{\rm ph}$ is the photospheric velocity of the SN, c is the speed of light, and $\beta_{\rm SN}\simeq 13.8$ is a constant (Arnett 1982). We assume that the

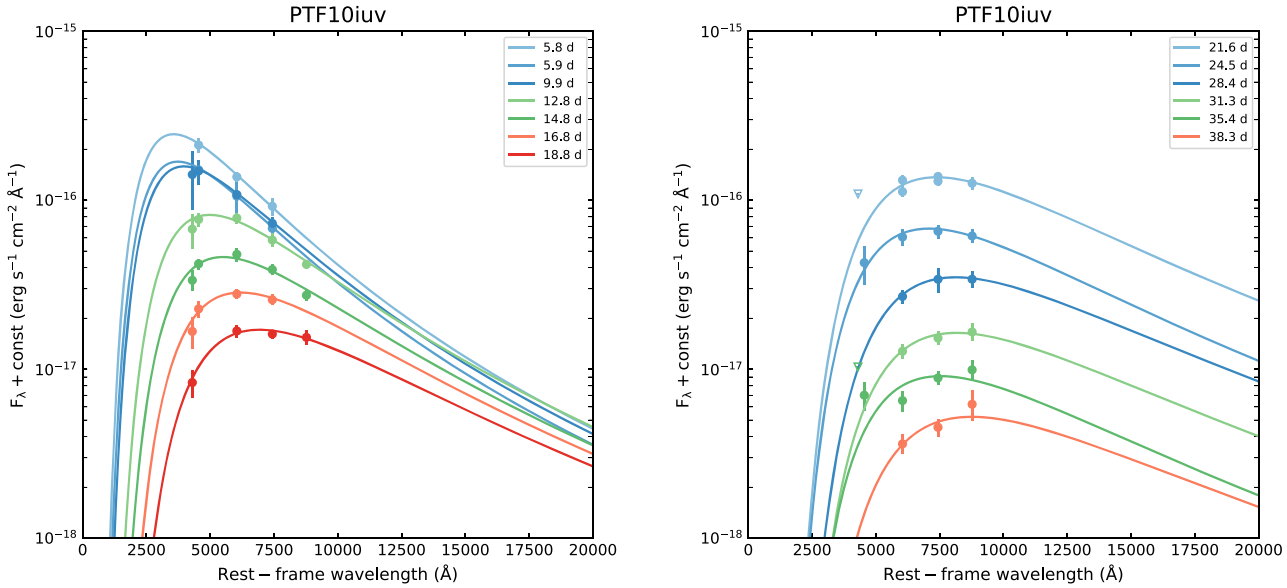

Figure 1. The blackbody fits of SEDs of PTF 10iuv. For clarity, the plots at all epochs have been shifted vertically.

Table 1
The Definitions, Units, Prior Ranges, Medians, 1σ Ranges, and Best-fitting Values (in Parentheses Following the Medians) of the Parameters for the ^{56}Ni Model

Parameter	Definition	Unit	Prior	Median (multi-band)	Median ($r-$band)
$M_{\rm ej}$	the ejecta mass	$M_\odot$	[0, 10.0]	$6.862^{+0.350}_{-0.350}$ (6.898)	$4.220^{+0.862}_{-0.732}$ (4.114)
$M_{\rm Ni}$	the ^{56}Ni mass	$M_\odot$	[0.0, 1.0]	$0.038^{+0.001}_{-0.001}$ (0.038)	$0.039^{+0.001}_{-0.001}$ (0.039)
κ	the optical opacity of the ejecta	cm^2 g^{-1}	[0.025, 0.25]	$0.025^{+0.000}_{-0.000}$ (0.025)	$0.040^{+0.009}_{-0.007}$ (0.040)
$T_{\rm f}$	the temperature floor	K	[1000, 10^4]	$3471.715^{+64.455}_{-54.229}$ (3471.515)	$3017.828^{+64.267}_{-59.940}$ (3037.006)
$t_{\rm shift}$	the explosion time relative to the first data	days	[−20, 0]	$-2.554^{+0.204}_{-0.212}$ (−2.556)	$-2.381^{0.280}_{-0.306}$ (−2.315)
χ^2/dof				11.549 (11.536)	1.508 (1.503)

early photosphere expansion velocity ($v_{\rm ph}$) of PTF 10iuv is a constant (10,000 km s^{-1}, Kasliwal et al. 2012). In the nebular phase, the bolometric luminosity of an SN is just the instantaneous power input, i.e., $L_{\rm SN}(t) = L_{\rm input}(t)$. We note that Arnett (1982) does not consider the γ-ray leakage effect, while all the input functions we use consider this.

We assume that the photosphere evolution can be described by the blackbody model. As affirmed in Figure 1, the spectral energy distributions (SEDs) of PTF 10iuv at all epochs having photometry in at least three bands can be described by the blackbody model. This indicates that the blackbody assumption is valid in these epochs. Furthermore, we assume that the late-time temperature ($T_{\rm f}$) is a constant (the temperature floor, Nicholl et al. 2017).

2.1. The ^{56}Ni Model

We first use the ^{56}Ni cascade decay model which is widely adopted to model the LCs of normal SNe Ib and Ic to fit the multi-band LCs of PTF 10iuv. The power input function ($L_{\rm input}(t)$) of ^{56}Ni cascade decay is from Valenti et al. (2008). In the ^{56}Ni model, the γ opacity (κ_γ) and positron opacity (κ_{e^+}) of the SN ejecta are set to be 0.027 and 7 cm^2 g^{-1} (e.g., Cappellaro et al. 1997; Mazzali et al. 2000; Maeda et al. 2003).

The definitions, the units, and the prior ranges of the free parameters of the ^{56}Ni model are listed in Table 1 (the 1st to 4th columns). In order to obtain the best-fitting values and 1σ ranges of the parameters, we use the Markov Chain Monte Carlo (MCMC) method by executing the `emcee` Python package (Foreman-Mackey et al. 2013).

The fit of the ^{56}Ni model can be found in Figure 2; the corresponding corner plot is presented in the upper panel of Figure A1. The medians, 1σ ranges, and the best-fitting values of the parameters are listed in Table 1 (the 5th column). We find the ^{56}Ni model fails to fit the LCs of PTF 10iuv, since the flux of the long plateau (138.8–290.3 days after the first data) in $r-$band is higher than that produced by the ^{56}Ni model.

Assuming that the flux of the last two data is from the host galaxy and, upon subtracting it from all r–band data (like Kasliwal et al. 2012), we find that the ^{56}Ni model can well fit

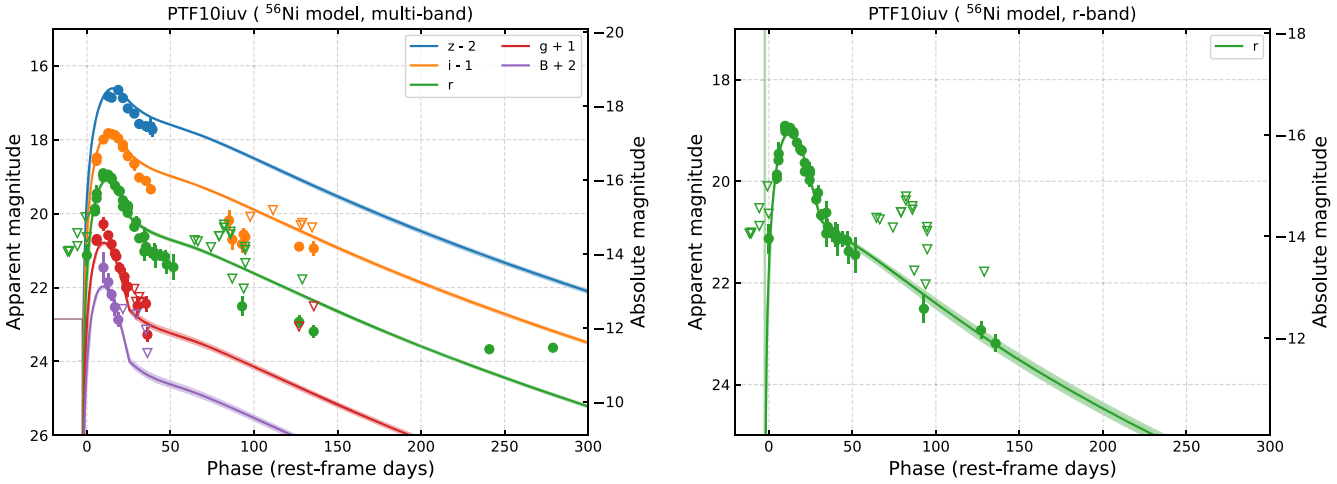

Figure 2. The fits of the multi-band LCs (the left panel) and r–band LC (the right panel, the late-time flux is assumed to be from the host galaxy and subtracted from the data at all epochs) of PTF 10iuv using the ^{56}Ni model. The shaded regions indicate 1σ bounds of the parameters. Triangles represent upper limits. The data are from Kasliwal et al. (2012).

the r–band LC of PTF 10iuv, see Figure 2 (the corresponding corner plot is presented in the lower panel of Figure A1; the medians, 1σ ranges, and the best-fitting values of the parameters are listed in the 6th column of Table 1). However, the derived $M_{\rm ej}$ is $4.22^{+0.86}_{-0.73}$ $M_{\odot}$; though it is lower than that ($6.862^{+0.350}_{-0.350}$) derived by the same model for the multi-band LCs of PTF 10iuv, it is significantly larger than 2.8 $M_{\odot}$ which is two times the Chandrasekhar mass and can be regarded as the upper limit of any WD-WD binary system. This indicates that PTF 10iuv might be a CCSN from the explosion of a massive star.

However, almost all confirmed CCSNe were not found in elliptical galaxies.[5] This, together with the fact that the distance between PTF 10iuv and its potential host galaxy (which is an elliptical galaxy) is very large (37 kpc), and the fact that the spectra of PTF 10iuv are different to those of typical SNe Ib disfavor the scenario that PTF 10iuv is a CCSN.

A larger value of κ would reduce $M_{\rm ej}$, but the larger leakage effect would result in a worse fit. This indicates that the assumption that the late-time flux was from the host galaxy cannot alleviate the problem of the ^{56}Ni model for fitting the LCs of PTF 10iuv. To fit the LCs of PTF 10iuv, more complicated models must be constructed. We no longer consider the possibility of host-galaxy contamination below.

2.2. The Four-element Model

The second possibility of the late-time excesses of the LCs of PTF 10iuv is that they were from the cascade decay of ^{44}Ti which is a long-lived radioactive element. In this scenario, the late-time LCs were mainly powered by ^{44}Ti and ^{56}Ni.

As demonstrated in the observations and numerical simulations, some other radioactive elements (e.g., ^{52}Fe, ^{48}Cr, ^{44}Ti) should also be produced by Ca-rich SNe. The contributions of the elements might exceed that of ^{56}Ni cascade decay in some epochs.

The numerical simulations of Waldman et al. (2011) include seven radioactive elements. To reduce the number of free parameters, we neglect the contributions from three elements (^{57}Ni, ^{51}Mn, and ^{49}Cr), and generalize the ^{56}Ni model to the one including four elements (^{56}Ni, ^{52}Fe, ^{48}Cr, and ^{44}Ti). It can be expected that the early-time LCs are mainly powered by ^{56}Ni, ^{48}Cr and ^{52}Fe, while the late-time LCs are mainly powered by ^{44}Ti in this model.

The power input function of the four-element model includes the contributions of ^{56}Ni, ^{52}Fe, ^{48}Cr, and ^{44}Ti. The input function of ^{44}Ti is from Equation (1) of Timmes et al. (1996); the value of κ_γ of ^{44}Ti is fixed to be 0.04 cm^2 g^{-1} (Timmes et al. 1996; Seitenzahl et al. 2014). The input functions of ^{52}Fe and ^{48}Cr are from equation (16) of Seitenzahl et al. (2014), with κ_γ fixed to be 0.027 cm^2 g^{-1} (Waldman et al. 2011).

The values of the half-life ($t_{1/2}$), the total energy radiated in gamma-rays Q_γ (or Q^γ in Seitenzahl et al. 2014), and the total energy liberated in the form of particles $Q_{\rm th}$ (or Q^l in Seitenzahl et al. 2014) of ^{52}Fe, ^{48}Cr, and ^{44}Ti are from Tables 3 and 4 of Dessart et al. (2014). The lifetime (τ) of ^{48}Cr and ^{44}Ti can be calculated by using $\tau = t_{1/2}/\ln 2$. The definitions, units, and prior ranges of the free parameters of the four-element model are listed in Table 2 (the 1st to 4th columns).

We find that the four-element model can fit the LCs of PTF 10iuv (see Figure 3). The medians, 1σ ranges, and the best-

[5] Based on observations of Lick Observatory Supernova Search (LOSS), Leaman et al. (2011) find that only 2.4% (13/536) of type II, Ib and Ic SNe exploded in early-type galaxies. Similarly, Irani et al. (2022) suggest that less than 1% of CCSNe in the local universe occur in elliptical galaxies.

Table 2
The Definitions, Units, Prior Ranges, Medians, 1σ Ranges, and Best-fitting Values (in Parentheses Following the Medians) of the Parameters for the Four-element Model

Parameter	Definition	Unit	Prior	Median
$M_{\rm ej}$	the ejecta mass	$M_\odot$	[0, 2.8]	$1.521^{+0.345}_{-0.254}$ (1.437)
$M_{\rm Ni}$	the ^{56}Ni mass	$M_\odot$	[0.0, 0.5]	$0.031^{+0.001}_{-0.003}$ (0.032)
$M_{\rm Ti}$	the ^{44}Ti mass	$M_\odot$	[0.0, 0.5]	$0.250^{+0.018}_{-0.018}$ (0.244)
$M_{\rm Cr}$	the ^{48}Cr mass	$M_\odot$	[0.0, 0.5]	$0.001^{+0.002}_{-0.001}$ (0.0004)
$M_{\rm Fe}$	the ^{52}Fe mass	$M_\odot$	[0.0, 0.5]	$0.046^{+0.016}_{-0.013}$ (0.045)
κ	the optical opacity of the ejecta	cm^2 g^{-1}	[0.025, 0.25]	$0.082^{+0.019}_{-0.017}$ (0.086)
$T_{\rm f}$	the temperature floor	K	[1000, 10^4]	$3386.016^{+63.756}_{-54.990}$ (3405.491)
$t_{\rm shift}$	the explosion time relative to the first data	days	[−20, 0]	$-0.916^{+0.130}_{-0.152}$ (−0.894)
χ^2/dof				1.831 (1.820)

fitting values of the parameters are listed in Table 2 (the 5th column); the corresponding corner plot is presented in Figure A2.

The derived parameters of the four-element model are $M_{\rm ej} = 1.521^{+0.345}_{-0.254}\ M_\odot$, $M_{\rm Ni} = 0.031^{+0.001}_{-0.003}\ M_\odot$, $M_{\rm Ti} = 0.250^{+0.018}_{-0.018}\ M_\odot$, $M_{\rm Cr} = 0.001^{+0.002}_{-0.001}\ M_\odot$, $M_{\rm Fe} = 0.046^{+0.016}_{-0.013}\ M_\odot$, $\kappa = 0.082^{+0.019}_{-0.017}$ cm^2 g^{-1}, $T_{\rm f} = 3386.016^{+63.756}_{-54.990}$ K, $t_{\rm shift} = -0.916^{+0.130}_{-0.152}$ days. The value of χ^2/dof is 1.831.

Using the best-fitting parameters, we can reproduce the theoretical bolometric LC of PTF 10iuv and derive the rise time $t_{\rm p}$ (13.90 days) and the peak luminosity $L_{\rm p}$ (8.15×10^{41} erg s^{-1}). The derived kinetic energy $E_{\rm k}$ ($E_{\rm k} = 0.3 M_{\rm ej} v_{\rm ph}^2$) of PTF 10iuv is 4.31×10^{50} erg.

2.3. The ^{56}Ni Plus CSI Model

Another promising scenario that can account for the late-time excesses of photometry involves the interaction between the ejecta and the circumstellar medium (CSM). In this scenario, the SN ejecta collide with the CSM, producing the forward and reverse shocks, converting a fraction of the kinetic energy of the ejecta to ultraviolet (UV)-optical-infrared (IR) radiation. The circumstellar interaction (CSI) provides additional energy sources for the SNe and increase their luminosity. The details of the CSI model can be found in Wang et al. (2019), which is based on Chevalier (1982), Chevalier & Fransson (1994), and Chatzopoulos et al. (2012). We assume that the photosphere expanded at the early-time epochs. The density profile of the CSM can be described by $\rho_{\rm CSM} = qr^{-s}$, where $q = \rho_{\rm CSM,1} r_1^s$, r_1 is the innermost radius of the CSM, and $\rho_{\rm CSM,1}$ is the density of the CSM at r_1. The CSM is a shell or a stellar wind when $s = 0$ or 2.

The fit using the four-element model shows that the early-time LCs are mainly powered by the cascade decay of ^{56}Ni, and the contributions of other radioactive species can be neglected. Therefore, we assume that the early-time LCs were powered by the cascade decay of ^{56}Ni, while the late-time LCs mainly were powered by the CSI triggered a few days after the explosion.

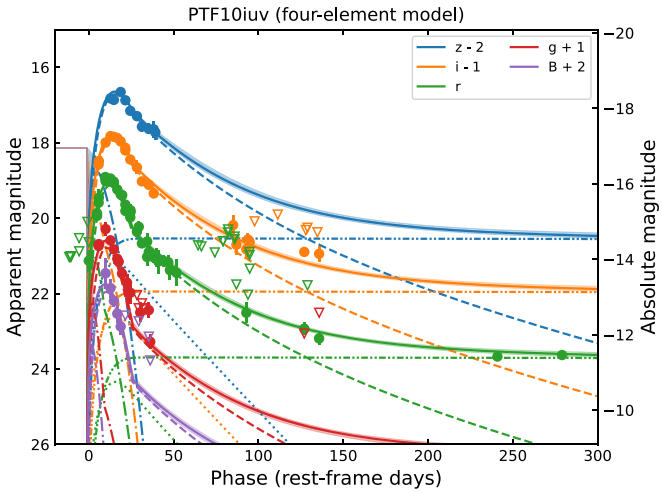

Figure 3. The fit of the multi-band LCs of PTF 10iuv using the four-element model. The dashed lines, dotted lines, dash–dotted lines, the dash-double-dotted lines, and the solid curves represent the contributions of ^{56}Ni, ^{48}Cr, ^{52}Fe, ^{44}Ti, and the sum of the four elements, respectively. The shaded regions indicate 1σ bounds of the parameters. Triangles represent upper limits. The data are from Kasliwal et al. (2012).

The contributions of other radioactive elements are neglected. The definitions, units, and prior ranges of the free parameters for the ^{56}Ni plus CSI model are listed in Table 3 (the 1st to 4th columns).

We find that the ^{56}Ni plus CSI model can fit the LCs of PTF 10iuv (see Figure 4). The medians, 1σ ranges, and the best-fitting values of the parameters for the case of $s = 0$ and $s = 2$ are listed in Table 3 (the 5th column and the 6th column); the corresponding corner plots are presented in Figures A3 and A4.

The derived parameters of the ^{56}Ni plus CSI model for the case of $s = 0$ ($s = 2$) are $M_{\rm ej} = 1.919^{+0.299}_{-0.412}$ ($0.777^{+0.101}_{-0.088}$) $M_\odot$, $M_{\rm Ni} = 0.035^{+0.001}_{-0.001}$ ($0.036^{+0.001}_{-0.001}$) $M_\odot$, $M_{\rm CSM} = 0.313^{+0.128}_{-0.214}$ ($0.408^{+0.067}_{-0.108}$) $M_\odot$, $\rho_{\rm CSM} = 32.339^{+38.536}_{-23.489}$ ($1.640^{+1.180}_{-0.642}$) $\times 10^{-15}$ g cm^{-3}, $\Delta t = 75.684^{+17.014}_{-23.504}$ ($46.001^{+17.140}_{-10.008}$) days,

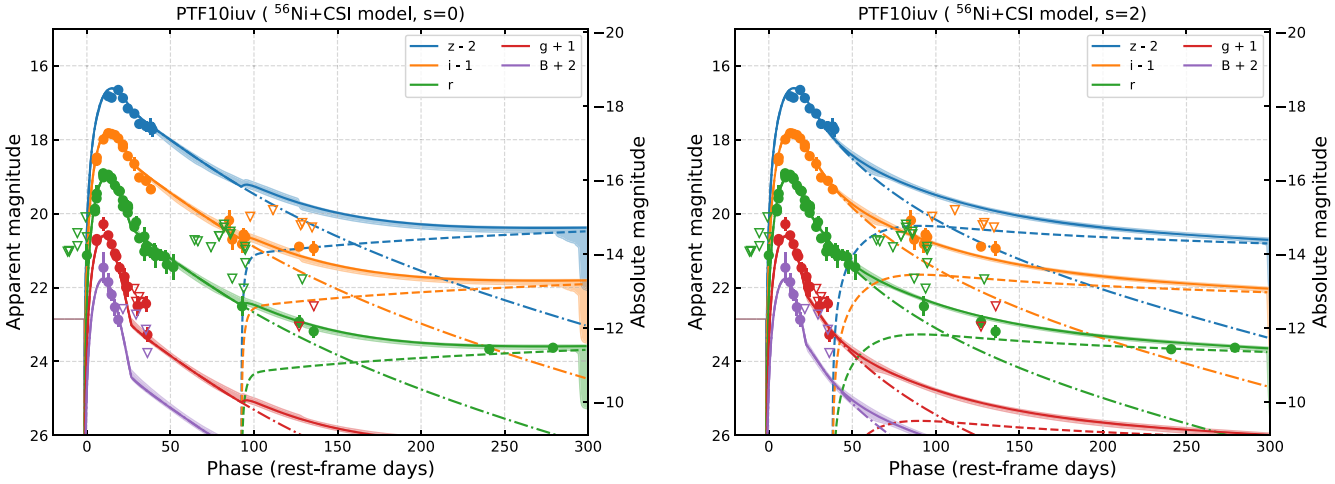

Figure 4. The fits of the multi-band LC of PTF 10iuv using the ^{56}Ni plus CSI models ($s = 0$, the left panel; $s = 2$, the right panel). The dashed lines, dash–dotted lines, and solid curves represent the contributions of CSI, ^{56}Ni, and the sum of the two energy sources, respectively. The shaded regions indicate 1σ bounds of the parameters. Triangles represent upper limits. The data are from Kasliwal et al. (2012).

Table 3
The Definitions, Units, Prior Ranges, Medians, 1σ Ranges, and Best-fitting Values (in Parentheses Following the Medians) of the Parameters for the ^{56}Ni Plus CSI Model

Parameter	Definition	Unit	Prior	Median ($s = 0$)	Median ($s = 2$)
$M_{\rm ej}$	The ejecta mass	$M_\odot$	[0, 2.8]	$1.919^{+0.299}_{-0.412}$ (2.102)	$0.777^{+0.101}_{-0.088}$ (0.782)
$M_{\rm Ni}$	The ^{56}Ni mass	$M_\odot$	[0, 0.5]	$0.035^{+0.001}_{-0.001}$ (0.035)	$0.036^{+0.001}_{-0.001}$ (0.036)
$M_{\rm CSM}$	The CSM mass	$M_\odot$	[0, 0.5]	$0.312^{+0.128}_{-0.214}$ (0.334)	$0.408^{+0.067}_{-0.108}$ (0.325)
$\rho_{\rm CSM}$	The CSM density	10^{-15} g cm^{-3}	[0.01, 100]	$32.339^{+38.536}_{-23.489}$ (42.794)	$1.640^{+1.180}_{-0.642}$ (1.280)
Δt	Time difference value	days	[30, 100]	$75.684^{+17.014}_{-23.504}$ (92.470)	$46.001^{+17.140}_{-10.007}$ (38.085)
ϵ	The conversion efficiency from kinetic energy to radiation		[0.1, 0.9]	$0.455^{+0.301}_{-0.226}$ (0.490)	$0.555^{+0.235}_{-0.270}$ (0.640)
x_0	Dimensionless radius		[0.01, 0.5]	$0.061^{+0.042}_{-0.013}$ (0.054)	$0.068^{+0.022}_{-0.013}$ (0.074)
κ	the optical opacity of the ejecta	cm^2 g^{-1}	[0.025, 0.25]	$0.064^{+0.020}_{-0.009}$ (0.057)	$0.162^{+0.028}_{-0.023}$ (0.161)
$T_{\rm f}$	the temperature floor	K	[1000, 10^4]	$3354.298^{+90.651}_{-49.735}$ (3332.641)	$3748.708^{+76.450}_{-83.315}$ (3759.749)
$t_{\rm shift}$	The explosion time relative to the first data	days	[−20, 0]	$-1.556^{+0.142}_{-0.149}$ (−1.546)	$-1.617^{+0.144}_{-0.155}$ (−1.634)
χ^2/dof				2.419(2.238)	1.938(1.928)

$\epsilon = 0.455^{+0.301}_{-0.226}$ $(0.555^{+0.235}_{-0.270})$, $x_0 = 0.061^{+0.042}_{-0.013}$ $(0.068^{+0.022}_{-0.013})$, $\kappa = 0.064^{+0.020}_{-0.009}$ $(0.162^{+0.028}_{-0.023})$ cm^2 g^{-1}, $T_{\rm f} = 3354.298^{+90.651}_{-49.735}$ $(3748.707^{+76.450}_{-83.315})$ K, $t_{\rm shift} = 1.556^{+0.142}_{-0.149}$ $(-1.617^{+0.144}_{-0.155})$ days. The values of χ^2/dof for the two cases are 2.419 and 1.938, respectively.

The $M_{\rm CSM}$ derived is ∼0.3 or 0.4 $M_\odot$. As shown in Dan et al. (2011), for a 0.5 and 1.2 $M_\odot$ WD system, only ∼3% of the mass of the secondary star (i.e., ∼0.015 $M_\odot$) is ejected from the merger. The fraction can be enhanced to be ∼10% (i.e., ∼0.05 $M_\odot$, Guerrero et al. 2004). The amount of CSM derived here is at least 10 times that derived from these two values, indicating that the this model is disfavored. Moreover, the absence of Hα emission lines in the nebular phases (Kasliwal et al. 2012) indicates that the CSM must be hydrogen poor. Assuming that the CSM was from a helium-rich companion via accretion or merger, the interaction between the ejecta and this amount of helium rich CSM would produce helium emission lines. However, Kasliwal et al. (2012) do not report the helium emission lines in the spectra. These suggest that it is difficult for the ^{56}Ni plus CSI model to account for the LCs of PTF 10iuv.

3. Discussion

3.1. The Nucleosynthesis and Main Energy Sources of PTF 10iuv

The derived $M_{\rm ej}$ of PTF 10iuv using the ^{56}Ni model is $6.86^{+0.35}_{-0.35}$ $M_\odot$ (for multi-band fit) or $4.22^{+0.86}_{-0.73}$ $M_\odot$ (for r–band

fit). Both the two values are significantly larger than the total masses of a WD-WD binary system, favoring the massive star explosion scenario. Section 2.1 demonstrates that the massive star scenario is disfavored. Additionally, the ^{56}Ni plus CSI model is also disfavored. Therefore, we no longer discuss these two models.

The derived $M_{\rm Ni}$ is $\sim$0.031 $M_{\odot}$, two times the value (0.016 $M_{\odot}$) derived by Kasliwal et al. (2012). The derived $M_{\rm Fe}$ and $M_{\rm Cr}$ are $\sim$0.046 $M_{\odot}$ and $\sim$0.001 $M_{\odot}$, respectively. The masses of ^{56}Ni and ^{48}Cr are roughly consistent with the numerical results of models of CO.55HE.2 and CO.6HE.2 in Waldman et al. (2011) (see the last columns of their Table 2). As mentioned above, however, the models in Waldman et al. (2011) suppose that only the helium shells are ejected, while our derived $M_{\rm ej}$ favors the scenario in which the carbon-oxygen (CO) WD is also blown up.

Although the derived $M_{\rm Fe}$ is slightly larger than $M_{\rm Ni}$, the contribution of ^{52}Fe is significantly lower than the latter. This is because the lifetimes of ^{52}Fe (0.498 days) and ^{52}Mn (0.022 days) are significantly shorter than those of ^{56}Ni (8.764 days) and ^{56}Co(111.424 days). The contribution of ^{48}Cr is also significantly lower than that of ^{56}Ni, due to its low yield ($\sim$0.001 $M_{\odot}$, which is $\sim 1/30$ times $M_{\rm Ni}$) and short lifetimes of ^{48}Cr (1.296 days) and ^{48}V (23.044 days). Therefore, the early-time LCs of PTF 10iuv were mainly powered by the cascade decay of ^{56}Ni. For comparison, the numerical simulation using CO.45HE.2 shows that the early-time LCs of SN 2005E were mainly powered by cascade decay of ^{48}Cr, rather than ^{56}Ni, ^{52}Fe or any other radioactive element (see Figure 4 of Waldman et al. 2011).

The fact that the early-time LCs of PTF 10iuv were mainly powered by ^{56}Ni indicates that the ^{56}Ni model can also account for the early-time LCs of of PTF 10iuv (but cannot fit the late-time LCs). Nevertheless, the four element model is necessary, since the ^{56}Ni model cannot constrain the masses of other radioactive species.

In the four-element model, the late-time LCs of PTF 10iuv were mainly powered by ^{44}Ti and ^{56}Ni. The contributions from ^{48}Cr and ^{52}Fe can be neglected. The value of ^{44}Ti mass of the four-element model is $0.250^{+0.018}_{-0.018}$ $M_{\odot}$, which is about 1/8 the ^{44}Ti mass ($\sim$2 $M_{\odot}$) estimated by Kasliwal et al. (2012). This discrepancy might be because Kasliwal et al. (2012) assume that all late-time flux was from the cascade decay of ^{44}Ti (in the scenario that the late-time flux was from ^{44}Ti), while our model includes the contribution from ^{56}Ni which can reduce the required $M_{\rm Ti}$.

The derived $M_{\rm Ti}$ is about 1.65–2 times the upper limit (0.14 $M_{\odot}$) of the numerical simulations performed for SN 2005E (Perets et al. 2010), or at least 50 times the ^{44}Ti values (which are of order $\sim 10^{-5}$–10^{-3} $M_{\odot}$) listed in Table 5 of Woosley & Kasen (2011).

Subtracting the host-galaxy contamination, which is unknown, can reduce the inferred ^{44}Ti mass. Besides, including the flux from other long-lived elements (e.g., ^{57}Co, ^{55}Fe, ^{60}Co) might also reduce the amount of ^{44}Ti. It is reasonable to regard the derived ^{44}Ti mass as an upper limit and assume that the real ^{44}Ti mass is (significantly) lower than the value derived by the model.

In general, high values of $M_{\rm Ti}$ are required for explaining the excesses relative to the LCs powered by ^{56}Ni and other short-lived radioactive elements at $\lesssim$100–200 days. Another example is the numerical modeling performed by Waldman et al. (2011) which shows that $\sim$1.65 $M_{\odot}$ of ^{44}Ti is needed for explaining the bolometric LC of SN 2005E $\sim$20–70 days after explosion (0.033×50, see model *a* of Figure 5 in Waldman et al. 2011 and the caption).

3.2. The Ejecta Mass and the Implication for the Explosion Mechanisms

The derived $M_{\rm ej}$ of the four-element model is $1.52^{+0.34}_{-0.25}$ $M_{\odot}$. Kasliwal et al. (2012) suppose that $t_{\rm r}$, which is the rise time, and v are respectively 12 days and 7600 km s^{-1}, which is the average photospheric velocity of PTF 10iuv. By using the relation $M_{\rm ej} \propto v t_{\rm r}^2$, and comparing the $M_{\rm ej}$ and v of PTF 10iuv to those of SNe Ia, they find that $M_{\rm ej}$ of PTF 10iuv is 0.46 $M_{\odot}$. By replacing 7600 with 10,000 km s^{-1} adopted here, the value of $M_{\rm ej}$ derived is 0.61 $M_{\odot}$, which is about half of the lower limit of our derived value.

Our derived $M_{\rm ej}$ is consistent with the $M_{\rm ej}$ of the merger of sub-Chandrasekhar WDs. Furthermore, it is larger than those of the ejected helium shells in the helium detonation scenario. This indicates that the explosion of the sub-Chandrasekhar WDs assumed to be the progenitor of PTF 10iuv left no remnant. For comparison, the numerical simulations for the bolometric LC of SN 2005E (Waldman et al. 2011) suggest that only the helium shell accreted from the companion was ejected, while the CO WD survived after the explosion.

4. Conclusions

In this paper, we model the LCs of PTF 10iuv, constraining the physical properties of its ejecta, the energy sources, as well as the explosion mechanisms. We find that the ^{56}Ni model and the ^{56}Ni plus CSI model cannot account for photometry of PTF 10iuv, and that the four-element (^{56}Ni, ^{48}Cr, ^{52}Fe, and ^{44}Ti) model can fit the LCs.

In the four-element model, the early-time LCs of PTF 10iuv were mainly powered by ^{56}Ni, and the contributions of ^{48}Cr and ^{52}Fe can be neglected. To explain the late-time LCs, $\sim$0.25 $M_{\odot}$ of ^{44}Ti is required. This value is rather high, and can be regarded as the upper limit of the real ^{44}Ti mass. We suggest that subtracting the contributions of the host-galaxy which is unknown and including the flux from some long-lived elements (^{57}Co, ^{55}Fe, ^{60}Co) can reduce the amount of ^{44}Ti. Therefore,

the derived ^{44}Ti can be regarded as an upper limit. The derived $M_{\rm ej}$ of the four-element model is $1.52^{+0.34}_{-0.25}$ $M_{\odot}$, consistent with the $M_{\rm ej}$ of the merger of sub-Chandrasekhar WDs.

We caution that one of the assumptions of our modeling is that the SEDs of PTF 10iuv at all epochs can be described by the blackbody function. We cannot verify whether this assumption is correct at the late-time epochs, since there are data in only one band (r–band). The modeling for a late-time r–band LC would be invalid if the late-time SEDs deviate from the blackbody function. This is the main caveat of our work. Besides, the possible host galaxy contamination prevents us from getting more accurate results.

The late-time multi-band photometric observations and the detailed modeling for the LCs can pose more stringent constraints on the precise values of ^{44}Ti mass of Ca-rich SNe. We expect that further observations for the late-time LCs of Ca-rich SNe and the modeling for the observations can constrain their nucleosynthesis, energy sources, as well as the explosion mechanisms.

Acknowledgments

This work is supported by National Natural Science Foundation of China (NSFC, grant Nos. 11963001, 12133003, 11833003, 11973020 (C0035736), and U1938201). This work is also supported by the Guangxi Talent Program ("Highland of Innovation Talents").

Appendix

Figures A1–A4 display the corner plots of the fits for the LCs of PTF 10iuv using the ^{56}Ni model, the four-element model, and the ^{56}Ni plus CSI model, respectively.

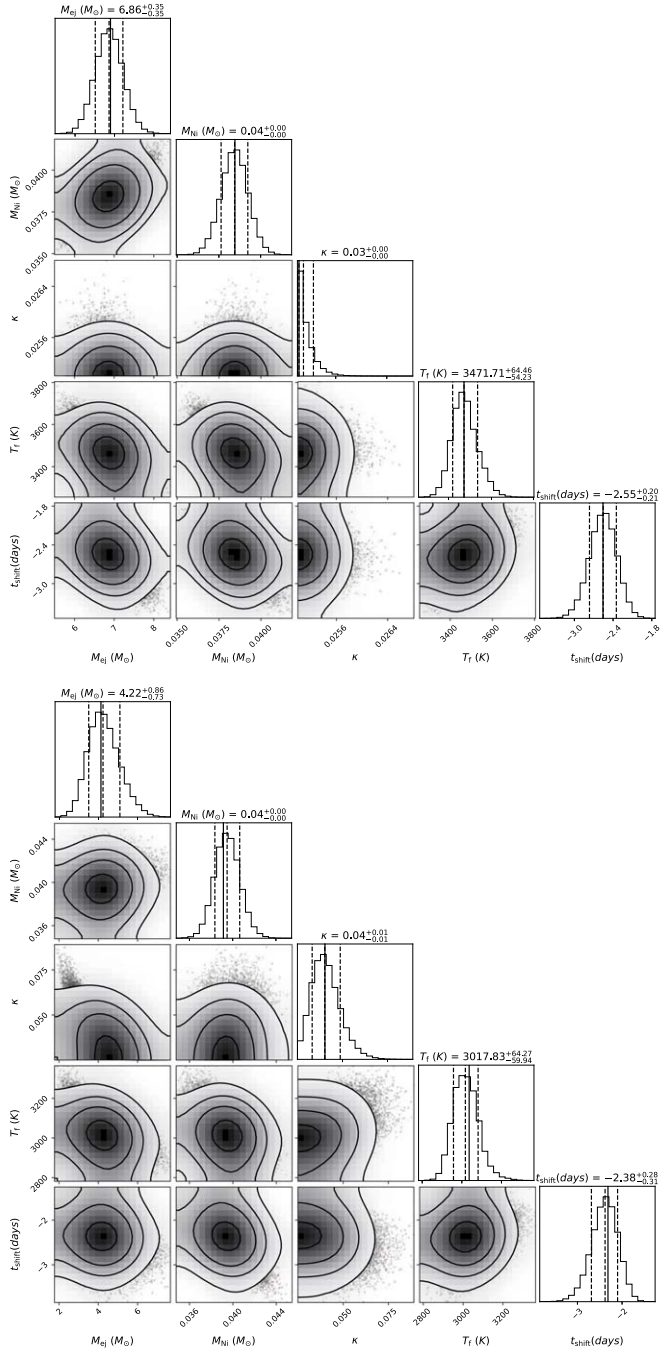

Figure A1. The corner plots of the ^{56}Ni model for the multi-band LCs (the upper panel) and *r*–band LC (the lower panel, the late-time flux had been subtracted) of PTF 10iuv. The solid vertical lines represent the best-fitting parameters, while the dashed vertical lines represent the medians and the 1σ bounds of the parameters.

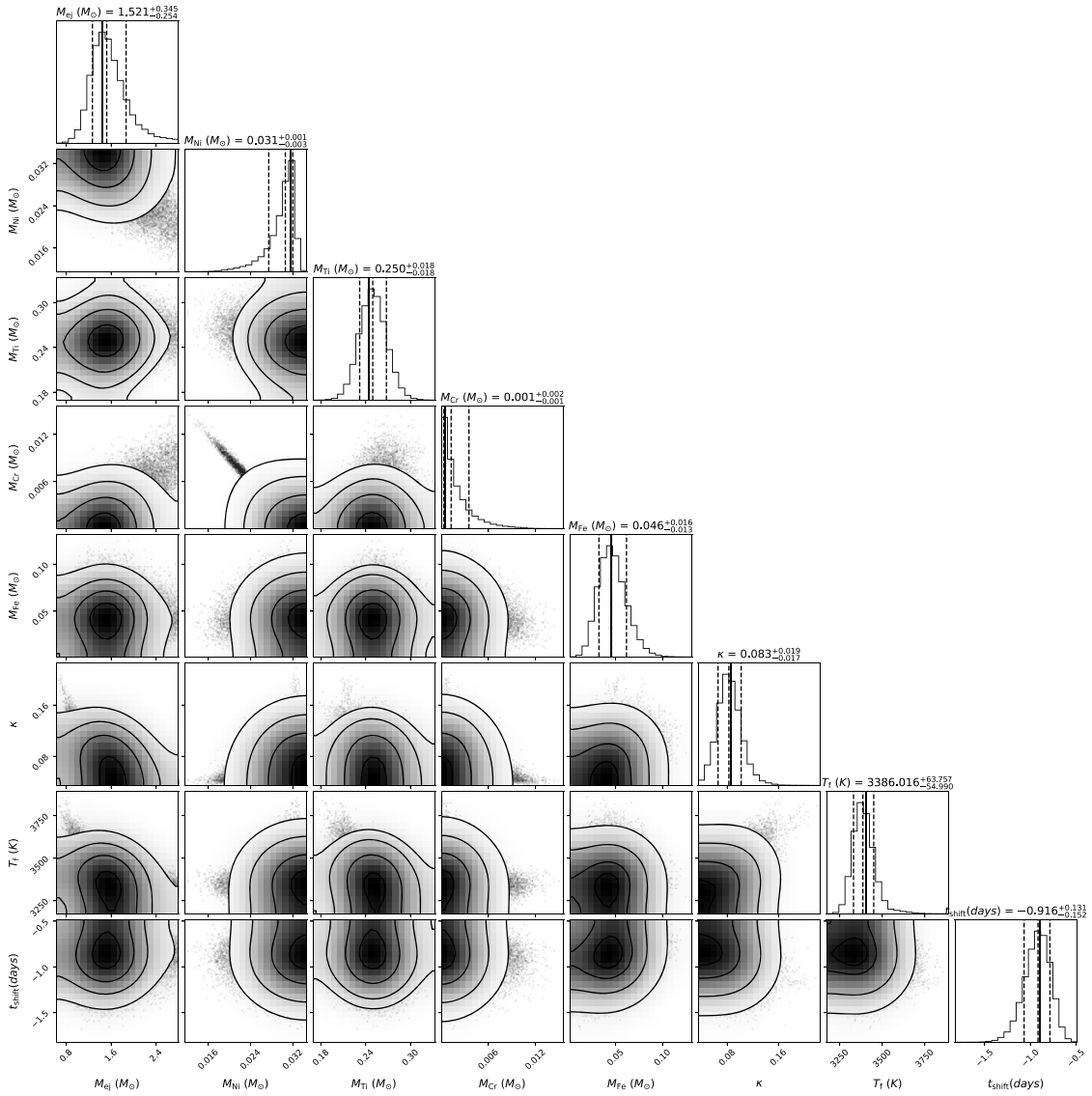

Figure A2. The corner plot of the four-element model for the multi-band LC of PTF 10iuv. The solid vertical lines represent the best-fitting parameters, while the dashed vertical lines represent the medians and the 1σ bounds of the parameters.

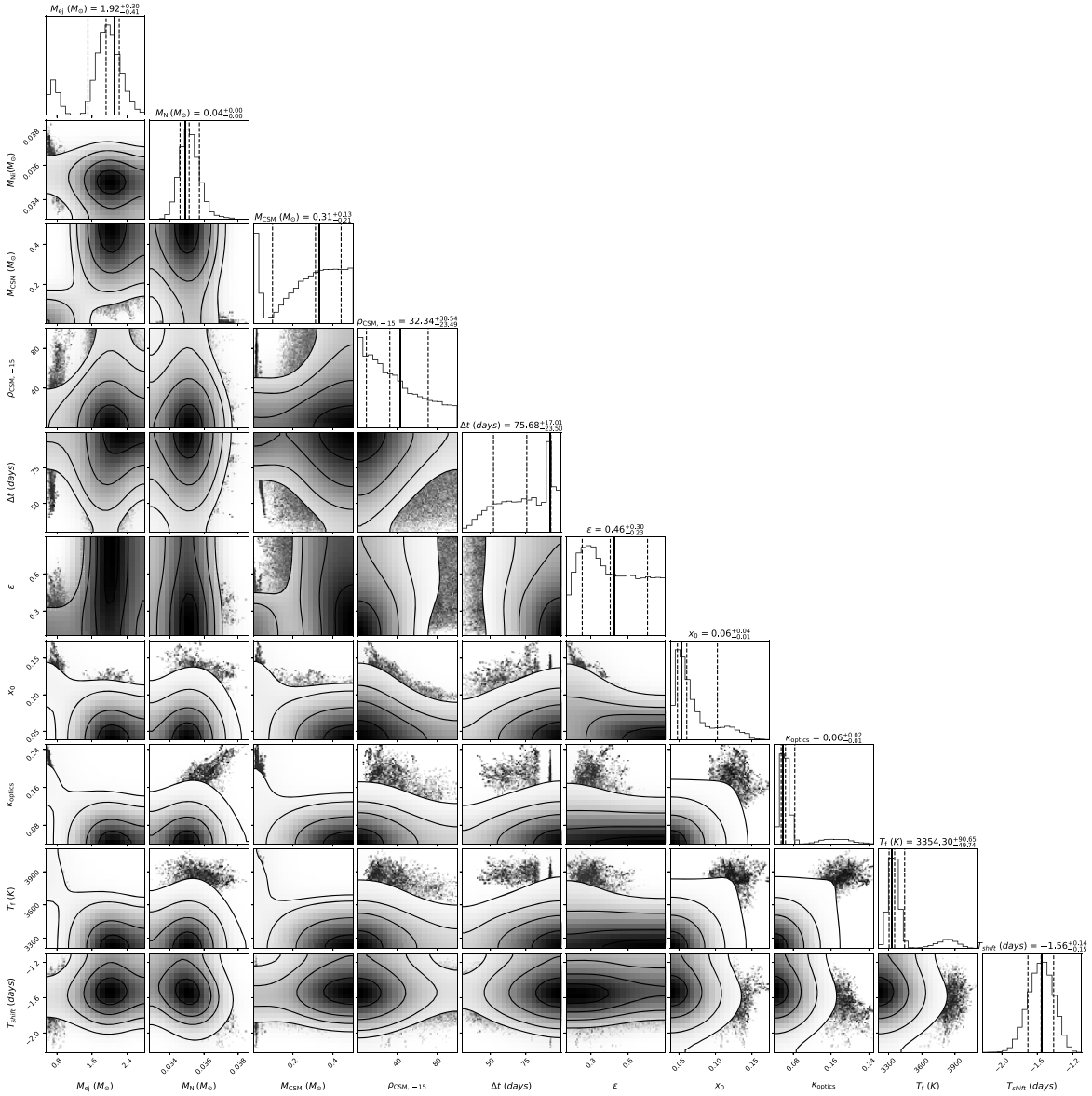

Figure A3. The corner plot of the ^{56}Ni plus CSI model ($s = 0$). The solid vertical lines represent the best-fitting parameters, while the dashed vertical lines represent the medians and the 1σ bounds of the parameters.

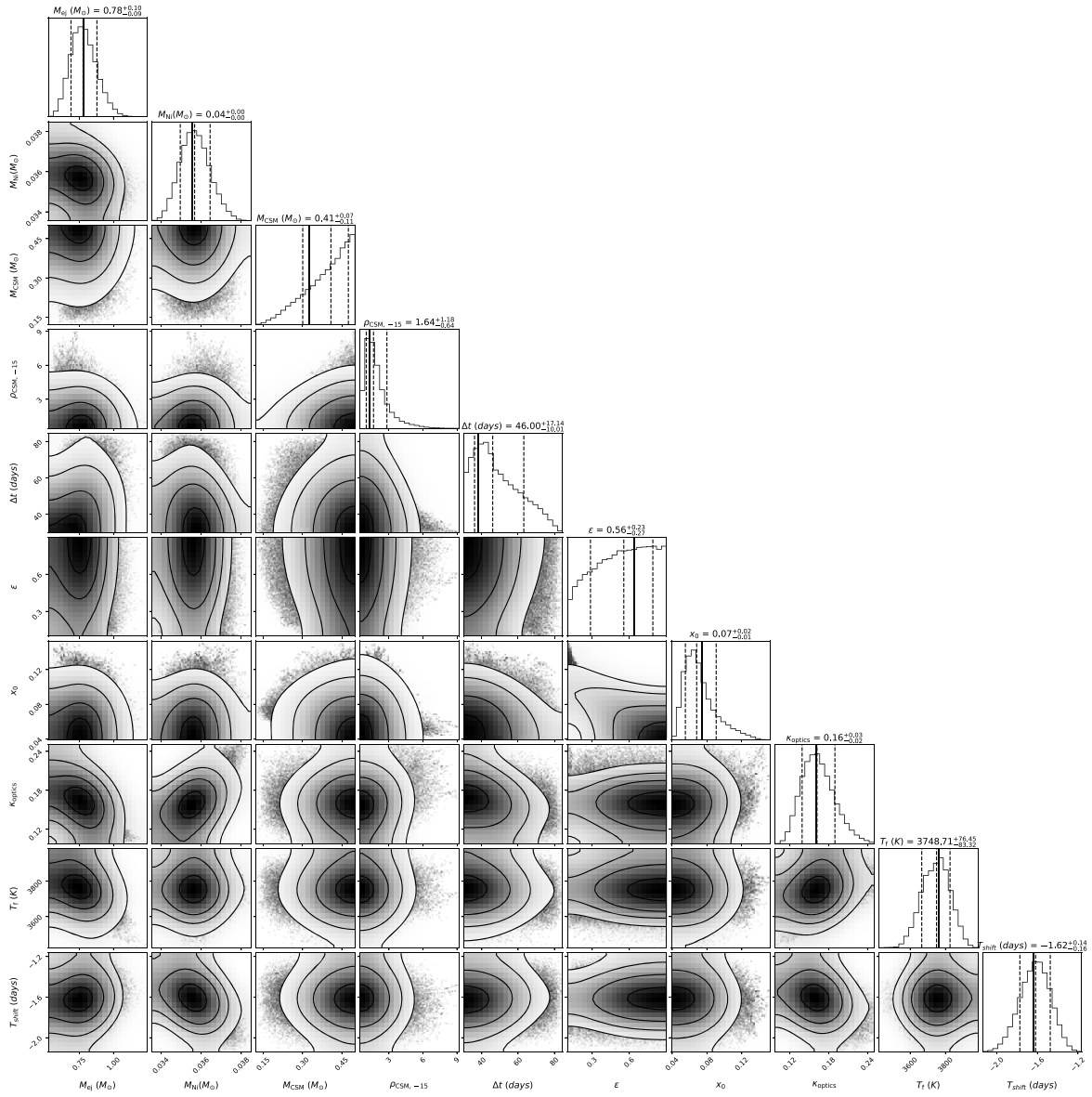

Figure A4. The corner plot of the ^{56}Ni plus CSI model ($s = 2$). The solid vertical lines represent the best-fitting parameters, while the dashed vertical lines represent the medians and the 1σ bounds of the parameters.

References

Aazami, A. B., & Li, W. D. 2001, IAUC, 7643, 2
Arnett, W. D. 1982, ApJ, 253, 785
Bildsten, L., Shen, K. J., Weinberg, N. N., & Nelemans, G. 2007, ApJL, 662, L95
Cao, Y., Kulkarni, S. R., Cook, D., et al. 2015, ATel, 8428
Cappellaro, E., Mazzali, P. A., Benetti, S., et al. 1997, A&A, 328, 203
Chatzopoulos, E., Wheeler, J. C., & Vinko, J. 2012, ApJ, 746, 121
Chen, P., Dong, S., Stritzinger, M. D., et al. 2020, ApJ, 889, L6
Chevalier, R. A. 1982, ApJ, 258, 790
Chevalier, R. A., & Fransson, C. 1994, ApJ, 420, 268
Chu, J., Li, W., Kloehr, W., et al. 2007, IAUC, 8875, 2
Dan, M., Rosswog, S., Guillochon, J., & Ramirez-Ruiz, E. 2011, ApJ, 737, 89
Das, K. K., Kasliwal, M. M., Fremling, C., et al. 2023, ApJ, 959, 12
De, K., Fremling, U. C., Gal-Yam, A., et al. 2021, ApJL, 907, L18
De, K., Kasliwal, M. M., Cantwell, T., et al. 2018, ApJ, 866, 72
De, K., Kasliwal, M. M., Tzanidakis, A., et al. 2020, ApJ, 905, 58
Dessart, L., Blondin, S., Hillier, D. J., et al. 2014, MNRAS, 441, 532
Dessart, L., & Hillier, D. J. 2015, MNRAS, 447, 1370
Dimai, A., Sehgal, A., Newton, J., et al. 2005, IAUC, 8569, 1
Drout, M. R., Soderberg, A. M., Mazzali, P. A., et al. 2013, ApJ, 774, 58
Ertini, K., Folatelli, G., Martinez, L., et al. 2023, MNRAS, 526, 279
Filippenko, A. V. 1997, ARA&A, 35, 309
Filippenko, A. V., Chornock, R., Swift, B., et al. 2003, IAUC, 8159, 2
Foley, R. J. 2015, MNRAS, 452, 2463
Foreman-Mackey, D., Hogg, D. W., Lang, D., et al. 2013, PASP, 125, 306
Gal-Yam, A. 2017, Handbook of Supernovae (Cham: Springer), 195
Graham, J., Li, W., Trondal, O., et al. 2005, IAUC, 8467, 1
Guerrero, J., García-Berro, E., & Isern, J. 2004, A&A, 413, 257

Irani, I., Prentice, S. J., Schulze, S., et al. 2022, ApJ, 927, 10
Irani, I., Chen, P., Morag, J., et al. 2024, ApJ, 962, 109
Jacobson-Galán, W. V., Margutti, R., Kilpatrick, C. D., et al. 2020b, ApJ, 898, 166
Jacobson-Galán, W. V., Polin, A., Foley, R. J., et al. 2020a, ApJ, 896, 165
Jacobson-Galán, Margutti, R., Kilpatrick, C. D., et al. 2021, ApJ, 908, L32
Kasliwal, M. M., Kulkarni, S. R., Gal-Yam, A., et al. 2012, ApJ, 755, 161
Kawabata, K. S., Maeda, K., Nomoto, K., et al. 2010, Natur, 465, 326
Leaman, J., Li, W., Chornock, R., & Filippenko, A. V. 2011, MNRAS, 412, 1419
Lee, M. G., Jang, I. S., & Kang, J. 2019, ApJ, 871, 33
Lunnan, R., Kasliwal, M. M., Cao, Y., et al. 2017, ApJ, 836, 60
Lyman, J. D., Levan, A. J., Church, R. P., et al. 2014, MNRAS, 444, 2157
Maeda, K., Mazzali, P. A., Deng, J., et al. 2003, ApJ, 593, 931
Mazzali, P. A., Iwamoto, K., & Nomoto, K. 2000, ApJ, 545, 407
Mazzali, P. A., Nomoto, K., Cappellaro, E., et al. 2001, ApJ, 547, 988
Moriya, T. J., Mazzali, P. A., Tominaga, N., et al. 2017, MNRAS, 466, 2085
Nicholl, M., Guillochon, J., & Berger, E. 2017, ApJ, 850, 55
Perets, H. B., Gal-Yam, A., Mazzali, P. A., et al. 2010, Natur, 465, 322
Planck Collaboration, Ade, P. A. R., Aghanim, N., et al. 2014, A&A, 571, A16
Prentice, S. J., Maguire, K., Flörs, A., et al. 2020, A&A, 635, A186
Puckett, T., & Dowdle, G. 2000, IAUC, 7507, 2
Puckett, T., Toth, D., Schwartz, M., et al. 2003, IAUC, 8117, 1
Pugh, H., & Li, W. 2003, IAUC, 8113, 2
Schlafly, E. F., & Finkbeiner, D. P. 2011, ApJ, 737, 103
Seitenzahl, I. R., Timmes, F. X., & Magkotsios, G. 2014, ApJ, 792, 10
Shen, K. J., & Bildsten, L. 2009, ApJ, 699, 1365
Shen, K. J., Kasen, D., Weinberg, N. N., et al. 2010, ApJ, 715, 767
Sullivan, M., Kasliwal, M. M., Nugent, P. E., et al. 2011, ApJ, 732, 118
Taubenberger, S. 2017, Handbook of Supernovae (Cham: Springer), 317
The, L.-S., Clayton, D. D., Diehl, R., et al. 2006, A&A, 450, 1037
Timmes, F. X., Woosley, S. E., Hartmann, D. H., et al. 1996, ApJ, 464, 332
Valenti, S., Benetti, S., Cappellaro, E., et al. 2008, MNRAS, 383, 1485
Valenti, S., Yuan, F., Taubenberger, S., et al. 2014, MNRAS, 437, 1519
Waldman, R., Sauer, D., Livne, E., et al. 2011, ApJ, 738, 21
Wang, L. J., Wang, X. F., Cano, Z., et al. 2019, MNRAS, 489, 1110
Woosley, S. E., & Kasen, D. 2011, ApJ, 734, 38
Zenati, Y., Perets, H. B., Dessart, L., et al. 2023, ApJ, 944, 22